ACS Sustainable Chemistry & Engineering

Research Article

pubs.acs.org/journal/ascecg

Unveiling Mesopore Evolution in Carbonized Wood: Interfacial Separation, Migration, and Degradation of Lignin Phase

Long Chen, Tuo Ji, Ruixia Yuan, Liwen Mu, Logan Brisbin, and Jiahua Zhu*

Intelligent Composites Laboratory, Department of Chemical and Biomolecular Engineering, The University of Akron, Akron, Ohio 44325, United States

Supporting Information

ABSTRACT: Carbon porous structure can be generated by an activation process, either chemically or physically. However, it remains a challenge to understand the pore structure evolution especially in a physically thermal oxidation process. In this work, mesopore evolution is revealed in association with three distinct stages: phase separation, migration, and thermal degradation. Oxidation temperature (270−370 °C) and time (1−7 h) are employed to study the microstructure evolution in oxidative environment. Various characterization techniques including scanning electron microscopy, transmission electron microscopy, N_2 adsorption−desorption, Raman and X-ray photoelectron spectroscopy have been used to investigate the structural and compositional change during thermal oxidation. High surface area mesoporous carbon is successfully manufactured from natural wood via this green technique, which could be applied to synthesize other highly porous carbon materials from similar biomass resources.

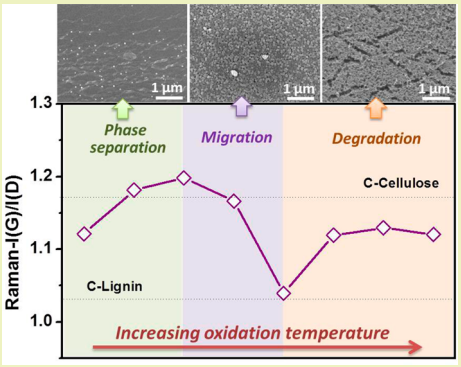

KEYWORDS: *Biomass, Lignin, Mesoporous carbon, Green process, Thermal oxidation*

INTRODUCTION

Porous carbon materials have attracted significant interest in the last a few decades due to their versatile applications in adsorption and separation,[1−4] catalysis,[5−8] energy storage/conversion,[9−13] and electrochemical sensors.[14] When rapid diffusion of molecules into a porous carbon internal surface is required especially in adsorption and catalytic reactions, the pore size and surface area need to be well controlled in a desired manner. The well-known template methods, either hard-template[15−20] or soft-template,[17,21−24] have been demonstrated to be very successful in controlling carbon pore size. However, the hard-template method is time-consuming, costly, and unsuitable for scale-up production. In particular, the necessity of removing the inorganic template by employing hazardous chemicals such as HF and NaOH is an unavoidable drawback. In soft-template method, the major concern comes from the utilization or the release of hazardous reactants such as formaldehyde and phenol. In fact, formaldehyde is often used as a cross-linking agent in mesoporous carbon (MC) synthesis, which is known to be carcinogenic and should be removed from industrial processes. Moreover, phenol is also carcinogenic and its derivatives are mostly toxic. Even though template methods provide a unique platform to control the pore structure, it remains a challenge to address the corresponding cost and environment related issues.

Utilizing lignocellulosic biomass (raw resources such as wood, cotton, or treated resources including cellulose, lignin, tannin, and starch) as a carbon precursor to synthesize porous carbon seems a promising approach.[19,25−27] By simply applying a carbonization process in an inert gas environment, solid carbon with possible rudimentary micropores could be produced, which is actually not practically useful in real applications. Larger pores will be required for diffusion and transport purposes. Conventionally, an activation process is usually adopted to open up the pore structure either chemically or physically. Chemical activation relies on the usage of a strong dehydrating agent, such as phosphorus pentoxide (P_2O_5), KOH, H_2SO_4, and zinc chloride ($ZnCl_2$).[28−30] Not only the corrosive feature of these chemicals, a washing process will be required to remove these chemicals which actually generates large amount of wastewater. Most of the existing physical activation processes are carried out at high temperatures of 800−1000 °C in the presence of steam and CO_2.[31−34] Besides the large energy consumption, carbon porosity control is relatively more difficult than that of a chemical activation method. Using thermal oxidative degradation seems more appealing because no chemicals will be involved and it requires relatively low temperature to burn out certain component and lead to pore formation. However, it is still a great challenge to control precisely the selective degradation without a fundamental understanding of pore structure evolution during thermal oxidation.

In this work, we first use natural soft wood as the starting material and process into carbon by a thermal annealing

Received: June 23, 2015
Revised: August 13, 2015
Published: August 26, 2015

DOI: 10.1021/acssuschemeng.5b00563
ACS Sustainable Chem. Eng. 2015, 3, 2489−2495

process in N_2 atmosphere. Then, thermal oxidation in air atmosphere with different processing temperatures and time is applied with the aim to create mesopores in carbon. Different from the conventional understanding of direct thermal degradation, three different structure evolution stages are discovered, which is phase separation, migration, and degradation of carbonized lignin from carbonized wood. Upon degradation of the relatively volatile component-carbonized lignin, at the final stage, cellulose-based highly porous carbon could be manufactured via this chemical-free process. Corresponding structural and compositional analysis are performed to understand the mesopore structure evolution process.

EXPERIMENTAL SECTION

Materials Preparation. Wood sample was collected from SPF (spruce-pine-fir) lumber. The composition is examined as 41.5% of cellulose, 24.7% hemicellulose, and 33.8% of lignin following Li's work.[35] SPF was cut into 3 × 3 × 10 mm small pieces and carbonized at 800 °C (heating rate: 5 °C min^{-1}) in nitrogen atmosphere for 2 h, and the product was named C-800. By applying a thermal oxidation process on C-800, carbon materials with different porous structures can be produced. Oxidation temperature and time are the two major factors those affect the final pore structure in oxidized carbon. The oxidation temperature is carefully selected within the range of 270–370 °C because material properties will not experience noticeable change when oxidized below 250 °C and white ashes will be observed due to overheating beyond 370 °C. With 5 h thermal heating in air, different porous carbon materials can be produced and named MC-T (T = 270, 300, 330, 340, 350, 360, and 370 °C). To study the oxidation time effect, C-800 was heated in air at 350 °C for 1, 3, 5, and 7 h and the products were named MC-1H, MC-3H, MC-5H and MC-7H.

Characterization. Thermal stability of C-800 and its oxidized form MC was studied by thermogravimetric analysis (TGA, TA Instruments Q500) in air atmosphere from 20 to 625 °C with a ramp rate of 5 °C min^{-1}. The morphology at cross section area and surface was characterized by scanning electron microscopy (SEM, JEOL-7401). Transmission electron microscopy (TEM) images of C-800, MC-330, and MC-360 were obtained by a JEOL JEM-1230 microscope operated at 120 kV. Samples for TEM observation were prepared by drying a drop of sample powder ethanol suspension on carbon-coated copper TEM grids. X-ray photoelectron spectroscopy (XPS) was accomplished using a PHI VersaProbe II Scanning XPS Microprobe with Al Kα line excitation source. Brunauer–Emmet–Teller (BET) surface area analysis of samples was performed using a TriStar II 3020 surface analyzer (Micromeritics Instrument Corp., USA) by N_2 adsorption–desorption isotherms. The average pore size was calculated by the Barret Joyner and Halenda (BJH) method from adsorption isotherm. Raman spectrum was obtained using a Horiba LabRam HR Micro Raman Spectrometer, equipped with a CCD camera detector within the range of 400–3000 cm^{-1}.

RESULTS AND DISCUSSION

The carbonized wood shows tightly adhered tubular cell arrays from a top view of the cross section area, Figure 1a. Focusing on a single cell, the schematic structure is presented in Figure 1b, where the tubular cells are closely packed with surrounding cells. C1, C2, and C3 represent three neighboring cells adhered together. Each cell is composed of cellulose framework, lignin, and hemicellulose. All the cells are strongly bonded with each other by the lignin lamella "glue" between the cells. Cellulose aggregates have an average diameter of 16 nm with elliptical spaces in-between having a length/width ratio of ~2 and a minor diameter across the ellipse of 5–10 nm.[36] These elliptical spaces constructed by cellulose/hemicellulose frame will be

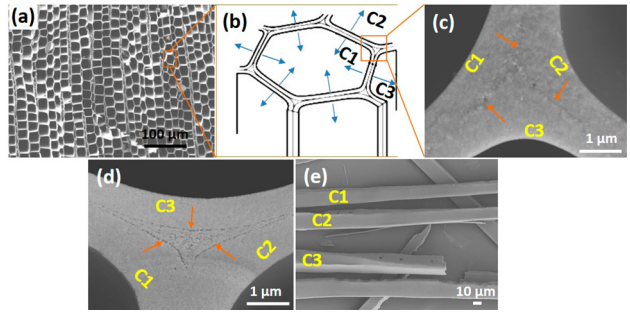

Figure 1. (a) cross section view of carbonized wood chunk with tubular cell arrays adhering to each other, (b) schematic structure of wood cells, (c and d) top-view SEM images at the interconnected area after thermal oxidation at 300 and 330 °C, and (e) side-view of the separated wood cell after 350 °C oxidation. C1, C2, and C3 represent the three adhered neighboring cells.

filled by lignin molecules afterward. From our previous work, the tubular cell array structure can be well remained after carbonizing the wood at 800 °C, Figure S1. Most of the previous study carried out the thermal oxidation at <300 °C, whereas it is not sufficient to generate structural change.[37] Microscale structure change has been rarely investigated by thermal oxidation at temperatures beyond 300 °C. Considering the nature of cellulose, hemicellulose and lignin molecules, the carbonized forms (C-cellulose, C-hemicellulose, and C-lignin) carry different physiochemical properties, e.g., thermal stability. By separating or removing one of the components in a designed thermal heating process, the carbon porous structure can be controlled in a desired manner. The structure change at the cross section area with increasing temperature from 300 to 350 °C clearly reveals the degradation of lignin lamella, Figure 1c–e. At 300 °C, the cells are still tightly bonded to each other, Figure 1c. A clear triangle-shaped void boundary was observed with increasing oxidation temperature to 330 °C, Figure 1d, indicating the degradation of lignin lamella was initiated. The cells were completely separated from each other by further increasing temperature to 350 °C, Figure 1e. These results confirmed C-lignin can be selectively degraded from carbonized wood by controlling oxidation temperature.

Besides the cell–cell adhesion area, structural change was also observed in the cell itself. Through characterizing the surface morphology change by SEM, Figure 2, the pore structure evolution was monitored with gradually increasing oxidation temperature from 300 to 370 °C. The temperature range was selected based on the thermal stability of the carbonized wood because white ash was observed in the product beyond 370 °C. Within the selected temperature range, the surface morphology showed two distinct stages. One is the enrichment of nanoparticles on the surface from 300 to 340 °C; the other is vanishing of nanoparticles and leaving porous texture from 350 to 370 °C. At the first stage, it is obvious that certain material migrated out of the bulk carbon phase (C-800) and aggregated on the surface in the form of spherical nanoparticles with uniform size of around 100 nm. At the second stage, these nanoparticles were thermally degraded at higher oxidation temperatures and the relatively stable carbon framework was well remained even heated at 370 °C. Apparent surface cracks were observed on MC-370 compared to MC-360, which is probably due to the partial degradation of carbon framework. From TEM study, the C-800 shows solid structure without pores, Figure 2g. By applying thermal heat at 330 and

DOI: 10.1021/acssuschemeng.5b00563
ACS Sustainable Chem. Eng. 2015, 3, 2489–2495

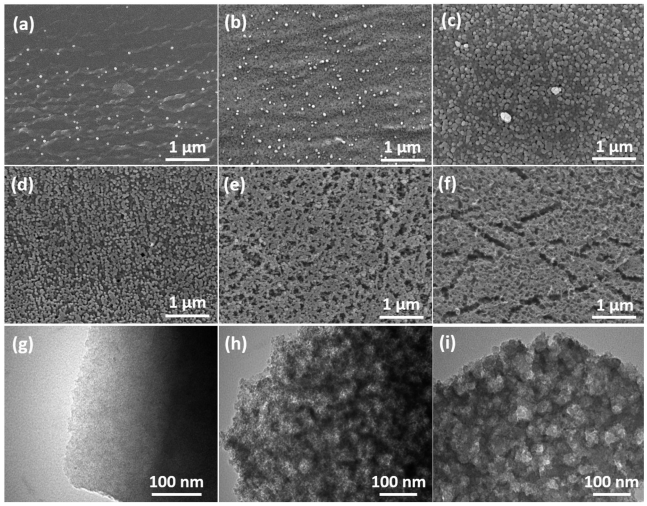

Figure 2. SEM surface microstructure of carbonized wood after thermal oxidation at different temperatures (a) MC-300, (b) MC-330, (c) MC-340, (d) MC-350, (e) MC-360, (f) MC-370. TEM images of (g) C-800, (h) MC-330, and (i) MC-360.

360 °C, obvious mesopore structures were successfully created. It is worth mentioning that the pore structure was created at early stage of nanoparticle migration even though the surface morphology does not show clear porous texture, Figure 2b,h. The pore size became larger at higher temperature.

Not only oxidation temperature but oxidation time also plays a significant role in the pore structure evolution process. As revealed in Figure 3, similar nanoparticle migration and

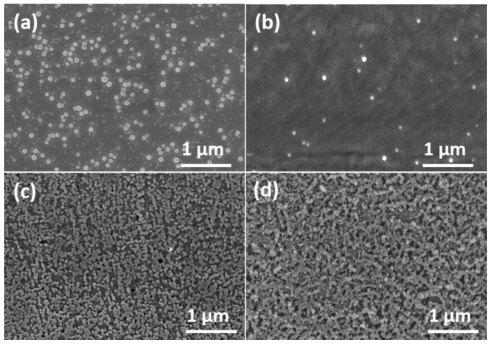

Figure 3. SEM surface microstructure of C-800 after thermal oxidation at 350 °C for different times (a) MC-1H, (b) MC-3H, (c) MC-5H, and (d) MC-7H.

degradation was observed in C-800 with heating durations of 1, 3, 5, and 7 h at 350 °C. With 1 h heating, the nanoparticles were migrated out and well distributed on the surface with 19% coverage. Most of the nanoparticles were degraded after 3 h of heating and only a few scarcely distributed nanoparticles remained, Figure 3b. Focusing on the relatively smooth surface beneath the nanoparticles, small slit pores or cracks are observed. With further extending the heating time to 5 h, the slit pores grow bigger and the surface texture shows a particle-chain structure with significant amounts of void spaces. These particle-chain structures are different from the aggregated nanoparticles observed at relative lower temperature, which can be attributed to the oxidized form of carbonized cellulose. With 7 h of heating, the chain structure becomes dominant, where the interpenetrating network formed eventually.

To investigate the pore structure evolution during thermal oxidation, N_2 adsorption−desorption analysis was performed, Figure 4a,b. The C-800 shows typical Type I isotherm with

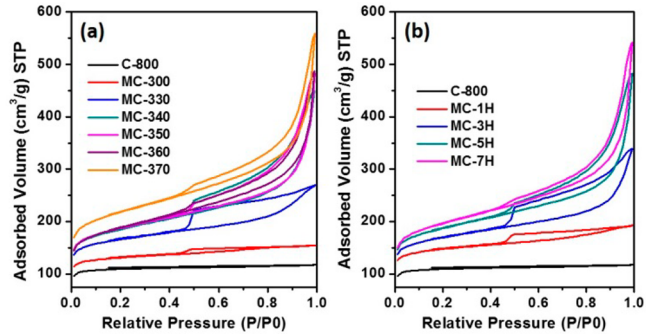

Figure 4. N_2 adsorption−desorption isotherms of carbons (a) oxidized at 300−370 °C for 5 h, (b) oxidized with different times (1−7 h) at 350 °C.

prominent adsorption at low relative pressures and then level off at higher relative pressure. Type I isotherm is usually considered to be indicative of adsorption in micropores (<2.0 nm).[38−40] Type IV hysteresis loops appeared after oxidation at different temperatures of 300−370 °C, signifying the formation of mesopores (2−50 nm). The hysteresis loops of MC-300 and MC-330 show type H4 feature and have been attributed to adsorption−desorption in narrow slit-like pores.[41] MC-340, MC-350, MC-360, and MC-370 exhibit type H3 feature, where the loops do not level off at relative pressure close to saturation pressure. A Type H3 loop was reported for materials comprised of aggregates of plate-like particles forming slit-like pores.[41] Time study shows a similar trend that H4 type loops formed with shorter oxidation time (MC-1H and MC-3H) and H4 → H3 type loop transition occurred with longer oxidation times (MC-5H and MC-7H). Before spherical nanoparticles migrated out of the bulk phase to surface, C-cellulose/C-lignin phase separation occurred first and slit-pores were formed at the boundary area. These results were consistent with SEM observation, where only small amount of nanoparticles appeared on the surface with majority remained in the bulk phase. Once the majority of flow phase migrated out to the surface, more internal spaces were created and subsequent structural change led to the type H4−H3 pore structure transition. The adsorption−desorption curves were almost overlapped for MC-340, MC-350, and MC-360, indicating the similar pore structure in these materials. Together with the SEM results in Figure 2c−e, it is highly possible that migration and degradation of flow phase occurred within the temperature range of 340−360 °C. Once migration is completed, the internal pore structure is fixed and thus similar adsorption−desorption curves were observed.

The BET surface area, average pore size and pore volume are summarized in Table 1. The total surface area gradually increased from 499 to 805 m^2/g with increasing oxidation temperature from 300 to 370 °C. Compared to C-800, the oxidation process at different temperatures increased the internal surface area (contributed by micropores) slightly by 4.8−12.6% whereas the external surface area was 1.1−6.7 times larger. A similar phenomenon was observed in samples with different heating times. The average pore size did not follow a linear pattern with oxidation temperature due to the existence of two contrary but simultaneous processes: one is new

DOI: 10.1021/acssuschemeng.5b00563
ACS Sustainable Chem. Eng. 2015, 3, 2489−2495

Table 1. Summary of N_2 Adsorption−Desorption Results

sample	S_{BET} (m^2/g)	$S_{BET(internal)}$ (m^2/g)	$S_{BET(external)}$ (m^2/g)	D_{pore} (nm)	V_{pore} (cm^3/g)
C-800	421	378	43	3.17	0.02
MC-300	499	409	90	3.64	0.06
MC-330	623	423	180	4.54	0.16
MC-340	686	418	268	4.51	0.24
MC-350[a]	694	426	268	4.47	0.24
MC-360	693	396	298	4.49	0.28
MC-370	805	473	332	4.53	0.31
MC-1H	557	434	123	4.12	0.09
MC-3H	633	427	206	4.38	0.18
MC-5H[a]	694	426	268	4.47	0.24
MC-7H	725	414	311	4.60	0.29

[a]MC-350 and MC-5H are the same sample.

micropore generation and the other is micropore growth into mesopore (or direct mesopore formation). The first process contributed to decrease the average pore size by generating small size pores while the second process did the opposite. The total pore volume increased monotonically with increasing temperature or heating time, indicating the well remained porous carbon frame without structural collapse.

To understand better the pore structure evolution during thermal oxidation, TGA analysis was performed on the carbon samples after oxidation at different temperatures. On the collected DTG curves in Figure 5a, two separated degradation

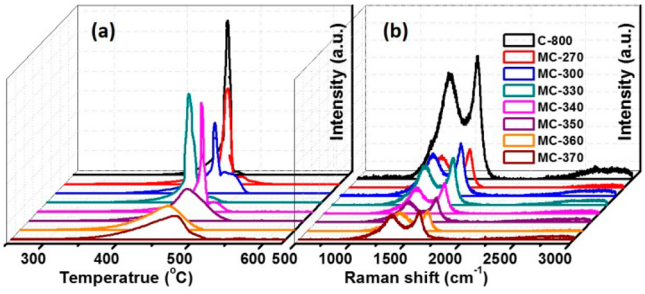

Figure 5. (a) DTG curves and (b) Raman spectrum of C-800 and MC-T (T = 270−370).

peaks were observed in MC-270, MC-300, MC-330, and MC-340, indicating the multiple components in the samples. These results were consistent with the SEM observation, where nanoparticles are separated from carbon bulk phase to form two different materials. After the complete degradation of nanoparticles at the temperature range of 350−370 °C, MC-350, MC-360, and MC-370 show only one broad degradation peak that is attributed to the degradation of the porous carbon frame.

All the above characterizations confirmed the nanoparticle migration from carbon bulk phase and subsequent degradation at elevated temperatures, which left the porous carbon texture behind. However, it is still not clear which component in the C-800 migrated out as nanoparticle and which component left behind to form the mesoporous carbon. It is well-known that cellulose and lignin are the major components in natural wood. Both can be converted to carbon by thermal annealing, while it remains a challenge to distinguish them through characterization techniques in the carbonized wood. Considering the physical nature of crystalline cellulose and amorphous lignin, we hypothesized that higher graphitization degree would be obtained in carbonized cellulose (C-cellulose) than that of carbonized lignin (C-lignin). Therefore, Raman technique was used to characterize both C-cellulose and C-lignin. The I(G)/I(D) ratio (G band intensity at 1605 cm^{-1}/D band intensity at 1335 cm^{-1})[42,43] is 1.17 and 1.03 (Figure S2) for C-cellulose and C-lignin, respectively, which is consistent with our hypothesis. However, it is worth mentioning that the I(G)/I(D) of C-cellulose might be underestimated since the cellulose molecular weight could be unavoidably decreased during the chemical extraction process. The graphitization degree will be negatively affected by the decreased molecular weight of cellulose.[44] With thermal oxidation at different temperatures, the I(G)/I(D) ratio changes significantly, Figure 5(b).

The I(G)/I(D) ratio as a function of oxidation temperature is summarized in Figure 6a. The change of I(G)/I(D) clearly

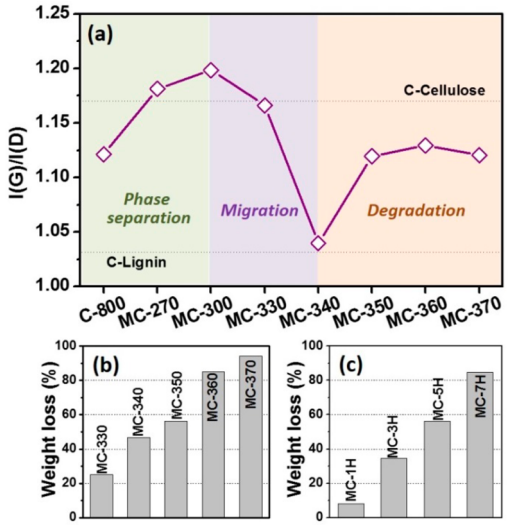

Figure 6. (a) I(G)/I(D) ratio of C-800 and MC-T (T = 270−370) from Raman spectrum, (b) weight loss of C-800 with thermal oxidation at different temperatures (T = 330, 340, 350, 360, and 370 °C; heating duration: 5 h), and (c) weight loss of C-800 with different oxidation time (1, 3, 5, and 7 h; T = 350 °C).

indicated the surface composition change, which serves as an index to identify the structural evolution. The I(G)/I(D) increased from 1.12 to 1.18 and 1.20 after oxidation at 270 and 300 °C. At this stage, phase separation occurred that exposed more C-cellulose component on the surface and leads to higher I(G)/I(D) ratios. The I(G)/I(D) values of MC-270 and MC-300 are larger than that of C-cellulose (1.17), indicating that the C-cellulose component in C-800 acquires a larger graphitization degree than the one carbonized after extraction. By further heating to 340 °C, nanoparticle migration became the dominant phenomena at this stage. Accompanied with the migration, I(G)/I(D) dropped down continuously to the lowest value of 1.04 that perfectly matched the 1.03 of C-lignin. Together with the SEM observation of MC-340, the aggregated nanoparticles on the fully covered surface could be identified as C-lignin. With further increasing oxidation temperature to the third stage (350−370 °C), the C-lignin nanoparticles degraded (partial C-cellulose degradation is possible) and I(G)/I(D) went up to 1.12−1.13 in MC-350, MC-360, and MC-370. The relatively lower I(G)/I(D) than that of C-cellulose is attributed to the $SP^2 \rightarrow SP^3$ carbon conversion.

DOI: 10.1021/acssuschemeng.5b00563
ACS Sustainable Chem. Eng. 2015, 3, 2489−2495

The carbon yield after specific thermal oxidation process was also monitored. The degradation of a specific component depends on both heating temperature and time. For example, with 5 h of heating, 350 °C seemed sufficient to degrade the C-lignin whereas not for C-cellulose, Figure 6b. Increasing the temperature to 360 and 370 °C, weight loss of >80% was observed indicating the degradation of C-cellulose, Figure 6c. While keeping at 350 °C for longer time, e.g., 7 h, C-cellulose degradation was also observed. In a word, thermal oxidation not only contributed to the degradation of less stable component but also involved gradual surface oxygenation that led to degradation on more stable component eventually.

To understand the surface property change together with the structural change, XPS characterization was performed on C-800, MC-330, and MC-360, Figure 7a. The atomic percentage

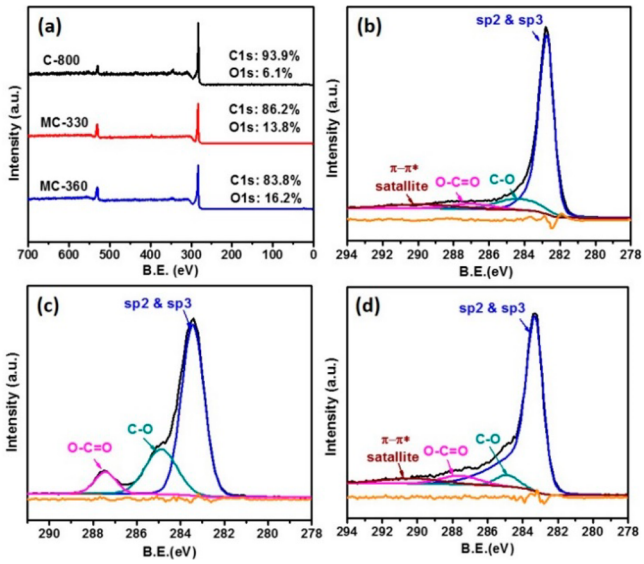

Figure 7. (a) XPS full scanned spectra of C-800, MC-330, and MC-360, C 1s deconvolution analysis of (b) C-800, (c) MC-330, and (d) MC-360.

of O 1s is 6.1% in C-800. After oxidation at 330 and 360 °C for 5 h, the atomic percent of O 1s increased to 13.8% and 16.2%, respectively. To quantify further the specific functional groups on the surface, C 1s spectrum was deconvoluted into three major bonding, C—C and C═C, C—O, and O—C═O. The area percentage of the deconvoluted peaks is summarized in Table 2. The area percentage of C—C and C═C, C—O, and

Table 2. Peak Deconvolution Results of C 1s for C-800, MC-330, and MC-360

	percentage of deconvoluted peaks (%)		
sample	C═C and C—C	C—O	O—C═O
C-800	82.69	12.03	5.28
MC-330	67.54	24.59	7.88
MC-360	59.01	32.22	8.76

O—C═O in C-800 was 82.7, 12.0, and 5.3%, respectively. The $\pi-\pi^*$ satellite peak appeared at 290.5 eV due to extended delocalized electrons in aromatic rings.[45,46] Also, the broad and asymmetric tail toward higher binding energy indicated a high concentration of C═C bonding in the sample. After oxidized at 330 and 360 °C, the area percent of C—C and C═C decreased to 67.5 and 59.0%, respectively. Meanwhile, the area percentage of oxygen-containing groups (C—O and O—C═O) increased significantly, which clearly indicated the severe surface oxygenation at elevated temperatures. The disappearance and appearance of $\pi-\pi^*$ satellite peaks in MC-330 and MC-360 is probably due to the migration (330 °C) and degradation (360 °C) of carbonized lignin.

CONCLUSIONS

In summary, a facile thermal oxidation method has been developed to process natural wood into high surface area mesoporous carbon materials. A unique transport phenomenon associated with carbonized lignin is observed during the oxidation process, which contributes to the pore structure evolution. The transport process experiences three distinct stages, e.g., phase separation of carbonized lignin from bulk carbon, migration to surface as spherical nanoparticles, and finally degradation. Together with the pore structure evolution, surface oxygenation on a porous carbon surface also occurred that introduces oxygen-containing functional groups. A carbon surface area of higher than 800 m^2/g is successfully synthesized from this green process. The interpenetrating porous feature of these materials ensures their promising applications in the fields of adsorption/separation, catalysis, and energy storage. More importantly, this technology could serve as a general tool to manufacture high surface area mesoporous carbons by using other similar biomass resources.

ASSOCIATED CONTENT

Supporting Information

The Supporting Information is available free of charge on the ACS Publications website at DOI: 10.1021/acssuschemeng.5b00563.

SEM cross section view of carbonized wood, Raman spectrum of carbonized cellulose and carbonized lignin (PDF).

AUTHOR INFORMATION

Corresponding Author

*J. Zhu. E-Mail: jzhu1@uakron.edu. Tel: 330-972-6859.

Notes

The authors declare no competing financial interest.

ACKNOWLEDGMENTS

This work is financially supported by the start-up fund of The University of Akron. Partial support from Faculty Research Committee, Biomimicry Research Incentive Center and Firestone Faculty Research Fellowship from The University of Akron are also acknowledged.

REFERENCES

(1) Hao, G.-P.; Jin, Z.-Y.; Sun, Q.; Zhang, X.-Q.; Zhang, J.-T.; Lu, A.-H. Porous carbon nanosheets with precisely tunable thickness and selective CO2 adsorption properties. *Energy Environ. Sci.* **2013**, *6* (12), 3740−3747.

(2) Li, Y.-Q.; Samad, Y. A.; Polychronopoulou, K.; Alhassan, S. M.; Liao, K. Carbon Aerogel from Winter Melon for Highly Efficient and Recyclable Oils and Organic Solvents Absorption. *ACS Sustainable Chem. Eng.* **2014**, *2* (6), 1492−1497.

(3) Ben, T.; Li, Y.; Zhu, L.; Zhang, D.; Cao, D.; Xiang, Z.; Yao, X.; Qiu, S. Selective adsorption of carbon dioxide by carbonized porous aromatic framework (PAF). *Energy Environ. Sci.* **2012**, *5* (8), 8370−8376.

DOI: 10.1021/acssuschemeng.5b00563
ACS Sustainable Chem. Eng. 2015, 3, 2489−2495

(4) Wu, Z.; Kong, L.; Hu, H.; Tian, S.; Xiong, Y. Adsorption Performance of Hollow Spherical Sludge Carbon Prepared from Sewage Sludge and Polystyrene Foam Wastes. *ACS Sustainable Chem. Eng.* **2015**, *3* (3), 552−558.
(5) Ji, T.; Chen, L.; Schmitz, M.; Bao, F. S.; Zhu, J. Hierarchical macrotube/mesopore carbon decorated with mono-dispersed Ag nanoparticles as a highly active catalyst. *Green Chem.* **2015**, *17* (4), 2515−2523.
(6) Ma, T. Y.; Dai, S.; Jaroniec, M.; Qiao, S. Z. Graphitic Carbon Nitride Nanosheet−Carbon Nanotube Three-Dimensional Porous Composites as High-Performance Oxygen Evolution Electrocatalysts. *Angew. Chem., Int. Ed.* **2014**, *53* (28), 7281−7285.
(7) Wang, L.; Wang, S.; Deng, X.; Zhang, Y.; Xiong, C. Development of Coconut Shell Activated Carbon-Tethered Urease for Degradation of Urea in a Packed Bed. *ACS Sustainable Chem. Eng.* **2014**, *2* (3), 433−439.
(8) Xu, X.; Li, Y.; Gong, Y.; Zhang, P.; Li, H.; Wang, Y. Synthesis of Palladium Nanoparticles Supported on Mesoporous N-Doped Carbon and Their Catalytic Ability for Biofuel Upgrade. *J. Am. Chem. Soc.* **2012**, *134* (41), 16987−16990.
(9) Merlet, C.; Rotenberg, B.; Madden, P. A.; Taberna, P.-L.; Simon, P.; Gogotsi, Y.; Salanne, M. On the molecular origin of supercapacitance in nanoporous carbon electrodes. *Nat. Mater.* **2012**, *11* (4), 306−310.
(10) Zhai, Y.; Dou, Y.; Zhao, D.; Fulvio, P. F.; Mayes, R. T.; Dai, S. Carbon Materials for Chemical Capacitive Energy Storage. *Adv. Mater.* **2011**, *23* (42), 4828−4850.
(11) Zhi, M.; Yang, F.; Meng, F.; Li, M.; Manivannan, A.; Wu, N. Effects of Pore Structure on Performance of An Activated-Carbon Supercapacitor Electrode Recycled from Scrap Waste Tires. *ACS Sustainable Chem. Eng.* **2014**, *2* (7), 1592−1598.
(12) Zhu, J.; Chen, M.; Yerra, N.; Haldolaarachchige, N.; Pallavkar, S.; Luo, Z.; Ho, T. C.; Hopper, J.; Young, D. P.; Wei, S.; Guo, Z. Microwave synthesized magnetic tubular carbon nanocomposite fabrics toward electrochemical energy storage. *Nanoscale* **2013**, *5* (5), 1825−1830.
(13) Shi, K.; Ren, M.; Zhitomirsky, I. Activated Carbon-Coated Carbon Nanotubes for Energy Storage in Supercapacitors and Capacitive Water Purification. *ACS Sustainable Chem. Eng.* **2014**, *2* (5), 1289−1298.
(14) He, X.; Zhou, L.; Nesterenko, E. P.; Nesterenko, P. N.; Paull, B.; Omamogho, J. O.; Glennon, J. D.; Luong, J. H. T. Porous Graphitized Carbon Monolith as an Electrode Material for Probing Direct Bioelectrochemistry and Selective Detection of Hydrogen Peroxide. *Anal. Chem.* **2012**, *84* (5), 2351−2357.
(15) Vinu, A.; Ariga, K.; Mori, T.; Nakanishi, T.; Hishita, S.; Golberg, D.; Bando, Y. Preparation and Characterization of Well-Ordered Hexagonal Mesoporous Carbon Nitride. *Adv. Mater.* **2005**, *17* (13), 1648−1652.
(16) Mane, G. P.; Talapaneni, S. N.; Anand, C.; Varghese, S.; Iwai, H.; Ji, Q.; Ariga, K.; Mori, T.; Vinu, A. Preparation of Highly Ordered Nitrogen-Containing Mesoporous Carbon from a Gelatin Biomolecule and its Excellent Sensing of Acetic Acid. *Adv. Funct. Mater.* **2012**, *22* (17), 3596−3604.
(17) Liang, C.; Li, Z.; Dai, S. Mesoporous Carbon Materials: Synthesis and Modification. *Angew. Chem., Int. Ed.* **2008**, *47* (20), 3696−3717.
(18) Böttger-Hiller, F.; Kempe, P.; Cox, G.; Panchenko, A.; Janssen, N.; Petzold, A.; Thurn-Albrecht, T.; Borchardt, L.; Rose, M.; Kaskel, S.; Georgi, C.; Lang, H.; Spange, S. Twin Polymerization at Spherical Hard Templates: An Approach to Size-Adjustable Carbon Hollow Spheres with Micro- or Mesoporous Shells. *Angew. Chem., Int. Ed.* **2013**, *52* (23), 6088−6091.
(19) Shopsowitz, K. E.; Hamad, W. Y.; MacLachlan, M. J. Chiral Nematic Mesoporous Carbon Derived From Nanocrystalline Cellulose. *Angew. Chem., Int. Ed.* **2011**, *50* (46), 10991−10995.
(20) Li, X.; Cao, Y.; Qi, W.; Saraf, L. V.; Xiao, J.; Nie, Z.; Mietek, J.; Zhang, J.-G.; Schwenzer, B.; Liu, J. Optimization of mesoporous carbon structures for lithium-sulfur battery applications. *J. Mater. Chem.* **2011**, *21* (41), 16603−16610.
(21) Zhai, Y.; Dou, Y.; Liu, X.; Park, S. S.; Ha, C.-S.; Zhao, D. Soft-template synthesis of ordered mesoporous carbon/nanoparticle nickel composites with a high surface area. *Carbon* **2011**, *49* (2), 545−555.
(22) Guo, B.; Wang, X.; Fulvio, P. F.; Chi, M.; Mahurin, S. M.; Sun, X.-G.; Dai, S. Soft-Templated Mesoporous Carbon-Carbon Nanotube Composites for High Performance Lithium-ion Batteries. *Adv. Mater.* **2011**, *23* (40), 4661−4666.
(23) Li, H.-Q.; Liu, R.-L.; Zhao, D.-Y.; Xia, Y.-Y. Electrochemical properties of an ordered mesoporous carbon prepared by direct tri-constituent co-assembly. *Carbon* **2007**, *45* (13), 2628−2635.
(24) Fang, Y.; Gu, D.; Zou, Y.; Wu, Z.; Li, F.; Che, R.; Deng, Y.; Tu, B.; Zhao, D. A Low-Concentration Hydrothermal Synthesis of Biocompatible Ordered Mesoporous Carbon Nanospheres with Tunable and Uniform Size. *Angew. Chem., Int. Ed.* **2010**, *49* (43), 7987−7991.
(25) Liu, R.-L.; Liu, Y.; Zhou, X.-Y.; Zhang, Z.-Q.; Zhang, J.; Dang, F.-Q. Biomass-derived highly porous functional carbon fabricated by using a free-standing template for efficient removal of methylene blue. *Bioresour. Technol.* **2014**, *154* (0), 138−147.
(26) Zhu, J.; Gu, H.; Guo, J.; Chen, M.; Wei, H.; Luo, Z.; Colorado, H. A.; Yerra, N.; Ding, D.; Ho, T. C.; Haldolaarachchige, N.; Hopper, J.; Young, D. P.; Guo, Z.; Wei, S. Mesoporous magnetic carbon nanocomposite fabrics for highly efficient Cr(VI) removal. *J. Mater. Chem. A* **2014**, *2* (7), 2256−2265.
(27) Wu, Z.-Y.; Li, C.; Liang, H.-W.; Chen, J.-F.; Yu, S.-H. Ultralight, Flexible, and Fire-Resistant Carbon Nanofiber Aerogels from Bacterial Cellulose. *Angew. Chem., Int. Ed.* **2013**, *52* (10), 2925−2929.
(28) Zhu, Y.; Murali, S.; Stoller, M. D.; Ganesh, K. J.; Cai, W.; Ferreira, P. J.; Pirkle, A.; Wallace, R. M.; Cychosz, K. A.; Thommes, M.; Su, D.; Stach, E. A.; Ruoff, R. S. Carbon-Based Supercapacitors Produced by Activation of Graphene. *Science* **2011**, *332* (6037), 1537−1541.
(29) Al Bahri, M.; Calvo, L.; Gilarranz, M. A.; Rodriguez, J. J. Activated carbon from grape seeds upon chemical activation with phosphoric acid: Application to the adsorption of diuron from water. *Chem. Eng. J.* **2012**, *203* (0), 348−356.
(30) Açıkyıldız, M.; Gürses, A.; Karaca, S. Preparation and characterization of activated carbon from plant wastes with chemical activation. *Microporous Mesoporous Mater.* **2014**, *198* (0), 45−49.
(31) Şahin, Ö.; Saka, C. Preparation and characterization of activated carbon from acorn shell by physical activation with H2O−CO2 in two-step pretreatment. *Bioresour. Technol.* **2013**, *136* (0), 163−168.
(32) Tsyntsarski, B.; Petrova, B.; Budinova, T.; Petrov, N.; Velasco, L. F.; Parra, J. B.; Ania, C. O. Porosity development during steam activation of carbon foams from chemically modified pitch. *Microporous Mesoporous Mater.* **2012**, *154* (0), 56−61.
(33) San Miguel, G.; Fowler, G. D.; Sollars, C. J. A study of the characteristics of activated carbons produced by steam and carbon dioxide activation of waste tyre rubber. *Carbon* **2003**, *41* (5), 1009−1016.
(34) Rodríguez-Reinoso, F.; Molina-Sabio, M.; González, M. T. The use of steam and CO2 as activating agents in the preparation of activated carbons. *Carbon* **1995**, *33* (1), 15−23.
(35) Li, S.; Xu, S.; Liu, S.; Yang, C.; Lu, Q. Fast pyrolysis of biomass in free-fall reactor for hydrogen-rich gas. *Fuel Process. Technol.* **2004**, *85* (8−10), 1201−1211.
(36) Salmen, L.; Olsson, A.-M.; Stevanic, H. S.; Simonovic, J.; Rasotic, K. Structural Organization of the Wood Polymers in the Wood Fiber Structure. *Bioresources* **2012**, *7*, 521−532.
(37) Szymański, G. S.; Karpiński, Z.; Biniak, S.; Świątkowski, A. The effect of the gradual thermal decomposition of surface oxygen species on the chemical and catalytic properties of oxidized activated carbon. *Carbon* **2002**, *40* (14), 2627−2639.
(38) Chen, B.; Ockwig, N. W.; Millward, A. R.; Contreras, D. S.; Yaghi, O. M. High H2 Adsorption in a Microporous Metal−Organic Framework with Open Metal Sites. *Angew. Chem.* **2005**, *117* (30), 4823−4827.

DOI: 10.1021/acssuschemeng.5b00563
ACS Sustainable Chem. Eng. 2015, 3, 2489−2495

(39) Su, F.; Poh, C. K.; Chen, J. S.; Xu, G.; Wang, D.; Li, Q.; Lin, J.; Lou, X. W. Nitrogen-containing microporous carbon nanospheres with improved capacitive properties. *Energy Environ. Sci.* **2011**, *4* (3), 717−724.
(40) Su, Y.-S.; Manthiram, A. Lithium−sulphur batteries with a microporous carbon paper as a bifunctional interlayer. *Nat. Commun.* **2012**, *3*, 1166.
(41) Kruk, M.; Jaroniec, M. Gas Adsorption Characterization of Ordered Organic−Inorganic Nanocomposite Materials. *Chem. Mater.* **2001**, *13* (10), 3169−3183.
(42) Zhu, J.; Wei, S.; Haldolaarachchige, N.; He, J.; Young, D. P.; Guo, Z. Very large magnetoresistive graphene disk with negative permittivity. *Nanoscale* **2012**, *4*, 152−156.
(43) Zhu, J.; Luo, Z.; Wu, S.; Haldolaarachchige, N.; Young, D. P.; Wei, S.; Guo, Z. Magnetic graphene nanocomposites: electron conduction, giant magnetoresistance and tunable negative permittivity. *J. Mater. Chem.* **2012**, *22* (3), 835−844.
(44) Kim, D.-Y.; Nishiyama, Y.; Wada, M.; Kuga, S. Graphitization of highly crystalline cellulose. *Carbon* **2001**, *39* (7), 1051−1056.
(45) Moreau, E.; Ferrer, F. J.; Vignaud, D.; Godey, S.; Wallart, X. Graphene growth by molecular beam epitaxy using a solid carbon source. *Phys. Status Solidi A* **2010**, *207* (2), 300−303.
(46) Fan, X.; Peng, W.; Li, Y.; Li, X.; Wang, S.; Zhang, G.; Zhang, F. Deoxygenation of Exfoliated Graphite Oxide under Alkaline Conditions: A Green Route to Graphene Preparation. *Adv. Mater.* **2008**, *20* (23), 4490−4493.

DOI: 10.1021/acssuschemeng.5b00563
ACS Sustainable Chem. Eng. 2015, 3, 2489−2495